ADVANCED OPTICAL MATERIALS
www.advopticalmat.de

Enhancing Chiroptoelectronic Activity in Chiral 2D Perovskites via Chiral–Achiral Cation Mixing

*Hao Li, Pranab Sarker, Xiaoyu Zhang, Maxwell W. Terban, Sanjit Ghose, Ibrahim Dursun, Mircea Cotlet, Mingxing Li, Yugang Zhang, Yuanze Xu, Shripathi Ramakrishnan, Tao Wei, Deyu Lu, and Qiuming Yu**

Rational design of chiral two-dimensional hybrid organic–inorganic perovskites is crucial to achieve chiroptoelecronic, spintronic, and ferroelectric applications. Here, an efficient way to manipulate the chiroptoelectronic activity of 2D lead iodide perovskites is reported by forming mixed chiral (R- or S-methylbenzylammonium (R-MBA$^+$ or S-MBA$^+$)) and achiral (*n*-butylammonium (*n*BA$^+$)) cations in the organic layer. The strongest and flipped circular dichroism signals are observed in (R/S-MBA$_{0.5}$*n*BA$_{0.5}$)$_2$PbI$_4$ films compared to (R/S-MBA)$_2$PbI$_4$. Moreover, the (R/S-MBA$_{0.5}$*n*BA$_{0.5}$)$_2$PbI$_4$ films exhibit pseudo-symmetric, unchanged circularly polarized photoluminescence peak as temperature increases. First-principles calculations reveal that mixed chiral–achiral cations enhance the asymmetric hydrogen-bonding interaction between the organic and inorganic layers, causing more structural distortion, thus, larger spin-polarized band-splitting than pure chiral cations. Temperature-dependent powder X-ray diffraction and pair distribution function structure studies show the compressed intralayer lattice with enlarged interlayer spacing and increased local ordering. Overall, this work demonstrates a new method to tune chiral and chiroptoelectronic properties and reveals their atomic scale structural origins.

1. Introduction

Chiral hybrid organic–inorganic perovskites have recently emerged as an appealing class of semiconducting materials because of their potential applications in chiroptoelecronics, spintronics, and ferroelectrics.[1] Two-dimensional chiral hybrid organic–inorganic perovskites (2D-CHOIPs) are a prime example of this emerging class,[2] in which an inorganic layer comprising the corner-sharing metal-halide octahedra is sandwiched between layers of chiral organic cations. The chirality of organic cations is considered to be transferred to the inorganic layers via hydrogen bonding between the $-NH_3^+$ of chiral organic cations and halides of $[MX_6]^{4-}$ octahedra (X = a halide anion; M = a divalent metal cation).[2,3] The resulting 2D-CHOIPs exhibit oppositely signed circular dichroism (CD) responses in the low-energy region due to the asymmetric absorption rates of left-handed and right-handed circularly polarized lights according to different Einstein coefficients possessed by the inorganic framework.[4] The chirality-induced spin-polarized band-splitting is responsible for such asymmetric absorption rate in 2D-CHOIPs. As such, the CD responses, such as the position, sign, and intensity of peaks or the chiroptical activity in 2D-CHOIPs, are governed by the underlying band structure, in particular, band gap, spin-polarized band splitting, and rotatory strength. Band engineering via chirality transfer is thus critical to tune the CD responses in 2D-CHOIPs.[5]

The strategies to manipulate the chirality transfer, and hence, band engineering, in 2D-CHOIPs are generally through varying either the inorganic sublattice[6] or the organic spacer layer.[7] An intriguing and unique way to manipulate the chirality transfer is to mix achiral and chiral organic cations in the organic layer. The

H. Li, X. Zhang, I. Dursun, Y. Xu, S. Ramakrishnan, Q. Yu
Robert Frederick Smith School of Chemical and Biomolecular Engineering
Cornell University
Ithaca, NY 14853, USA
E-mail: qy10@cornell.edu

P. Sarker, T. Wei
Department of Chemical Engineering
University of South Carolina
Columbia, SC 29208, USA

The ORCID identification number(s) for the author(s) of this article can be found under https://doi.org/10.1002/adom.202401782

DOI: 10.1002/adom.202401782

M. W. Terban
Max Planck Institute for Solid State Research
Heisenbergstraße 1, 70569 Stuttgart, Germany

S. Ghose
National Synchrotron Light Source II
Brookhaven National Laboratory
Upton, NY 11973, USA

M. Cotlet, M. Li, Y. Zhang, D. Lu
Center for Functional Nanomaterials
Brookhaven National Laboratory
Upton, NY 11973, USA

T. Wei
Department of Biomedical Engineering
University of South Carolina
Columbia, SC 29208, USA

CD signals are not only enhanced but also flipped sign simply by blending chiral and achiral cations.[8] 2D-CHOIPs with a broad array of chiral and achiral organic cations are investigated using the crystallographic and first-principles methods.[5] The study shows that a specific bond angle disparity associated with asymmetric tilting distortions of the metal halide octahedra breaks local inversion symmetry and is strongly correlated with the computed spin-splitting. This result indicates that local distortions in the inorganic layer induced by an appropriate choice of organic cations provide a key design rule to achieve strong spin-splitting in 2D-CHOIPs.

Apart from the controlled spin-splitting, the stability of photoluminescence is another key optoelectronic component for the application of chiral perovskites in optoelectronic devices. In 2D perovskites, it has been demonstrated that the temperature-dependent emission peak was affected by the synergetic effect of thermal expansion and electron−phonon interaction.[9] All existing chiral and achiral 2D perovskites exhibit a peak shift with changing temperatures.[10] Since the peak shift reflects the dynamic changes of color purity and color gamut with the changing external conditions, a simple, common strategy to enhance the color stability is highly needed. To address this issue, a systematic investigation of the impact of chiral and achiral cations, as well as their mixtures, on thermal expansion interaction and electron−phonon interaction is required.

Density-functional theory (DFT) is a powerful method to investigate the effect of chirality-induced inversion asymmetry on the electronic structures and has been successfully used to predict a substantial bulk Rashba-Dresselhaus splitting in the inorganic-derived conduction band, which is absent in the racemic analog.[3] The crystal structures and electronic band structures obtained from DFT calculations can help to establish the structure–property relationship for 2D-CHOIPs and accelerate their rational designs. However, despite recent explorations on both experimental and theoretical fronts, the rational design of 2D-CHOIPs is still in its infancy because the structure–property relationship for 2D-CHOIPs has not been fully understood. In addition, the limited choice of chiral organic cations and weak chirality greatly hinder their chiral optoelectronic applications, such as emission[11] and detection of CPL.[12] Also, most of the existing methods only focus on varying the strength of the CD signal but not on the chiroptoelectronic activity. Thus, conducting a comprehensive and synergetic experiment-theory study is imperative to reveal the structure–property relationship of 2D-CHOIPs, which is the cornerstone to fulfill the promises of future chiral optoelectronic applications.

In this work, we manipulate the chirality of 2D-CHOIPs by blending achiral cation (*n*-butylammonium, nBA$^+$) and chiral cation (R/S-MBA$^+$) to form ((R/S-MBA)$_{1-x}$$nBA_x$)$_2PbI_4$ 2D-CHOIPs and perform a systematic and comprehensive investigation of the relationship between structure and chiroptoelectronic properties. By partial substitution of chiral cations with achiral cations, we demonstrate an effective strategy to tune the polarity and intensity of the CD signal. Additionally, we conduct DFT calculations to investigate the crystal structures, hydrogen bonding, and band structures. We find that incorporating achiral cations into the chiral organic spacer layer results in stronger and more asymmetric hydrogen bonding, larger octahedral distortion, and rigid crystal structure. We also carry out temperature-dependent powder X-ray diffraction (PXRD), pair distribution function (PDF) analysis, and circularly polarized photoluminescence (CPPL) measurements to understand the structure–chiroptoelectronic property relationship. Local structure characterization of the PDFs suggests that the presence of mixed cations increases local ordering, particularly at low temperatures. The fixed peak position and only slightly asymmetric peak broadening with increasing temperature exhibited in the CPPL spectra of (R/S-MBA$_{0.5}$$nBA_{0.5}$)$_2PbI_4$ suggest that the presence of mixed cations impacts the nature of electron–phonon coupling. Our work thus sheds light on the manipulation of chiroptoelectronic properties of 2D-CHOIPs via a simple yet powerful method.

2. Results and Discussion

2.1. Chiral Optical Activity and Crystal Structure

To investigate how mixing achiral cations with chiral cations in the organic layer affects the chirality of the 2D-CHOIPs, we fabricated a series of 2D-CHOIP thin films with the formula of (R/S-MBA$_{1-x}$$nBA_x$)$_2PbI_4$, where x = 0, 0.1, 0.2, 0.5, 0.7, 0.9, and 1.0, as well as racemic 2D perovskite (rac-MBA)PbI$_4$ thin films using one-step spin-coating method.[6a] We confirmed that all the thin films adopted layered structures with blending of chiral and achiral ammonium ions sitting in between [PbI$_4$]$^{2-}$ sheets by X-ray diffraction (XRD) (Figure S1a,b and Table S1, Supporting Information). All the samples exhibit a set of strong 00l reflections with the (001) peak located between the 2θ angle of 6°–7°, demonstrating the formation of the inorganic layers intercalated by the organic cations. The UV–vis absorption spectra exhibit a strong exciton peak around 500 nm, characterizing 2D Ruddlesden–Popper phase. The exciton peak appears at 498 nm for the (R/S-MBA)$_2$PbI$_4$ thin films (**Figure 1a**,) and gradually red shifts with the increase of the nBA$^+$ fraction to 514 nm for the (nBA)$_2$PbI$_4$ film (Figure S1c, Supporting Information).

We collected CD spectra to investigate their chiral optical activities. The CD spectra display a distinct derivative feature for the (R/S-MBA)$_2$PbI$_4$ films, while the (rac-MBA)$_2$PbI$_4$ film exhibits no CD signal (Figure 1c,d). The low energy CD signals around 500 nm can be assigned to the optical activities within the inorganic framework induced by chiral cations (R/S-MBA$^+$), which results from the Cotton effect.[13] By incorporating achiral nBA$^+$ cations, the CD signal gradually changes from positive to negative, except for the R-MBA/nBA molar ratios of 1:9 and 0:10, where the weak signal intensity made the identification of opposite polarity ambiguous (Figure S1d, Supporting Information). The CD signals of (R/S-MBA$_{0.5}$$nBA_{0.5}$)$_2PbI_4$ films are not only flipped in sign in comparison to (R/S-MBA)$_2$PbI$_4$ but also enhanced to ≈±100 mdeg, with a magnitude about five times greater than that of (R/S-MBA)$_2$PbI$_4$ (Figure 1c,d).

We calculated the anisotropy factor (g_{CD})[14] and obtained g_{CD} of 2.61×10^{-4} and -2.91×10^{-4} for the (R/S-MBA)$_2$PbI$_4$ films, respectively, which are close to the reported values.[14] In contrast, the (R/S-MBA$_{0.5}$$nBA_{0.5}$)$_2PbI_4$ films show almost one order of magnitude larger g_{CD} of -1.92×10^{-3} and 1.56×10^{-3}, respectively. The substantially higher g_{CD} value and opposite polarity indicate that the incorporation of achiral organic cations to

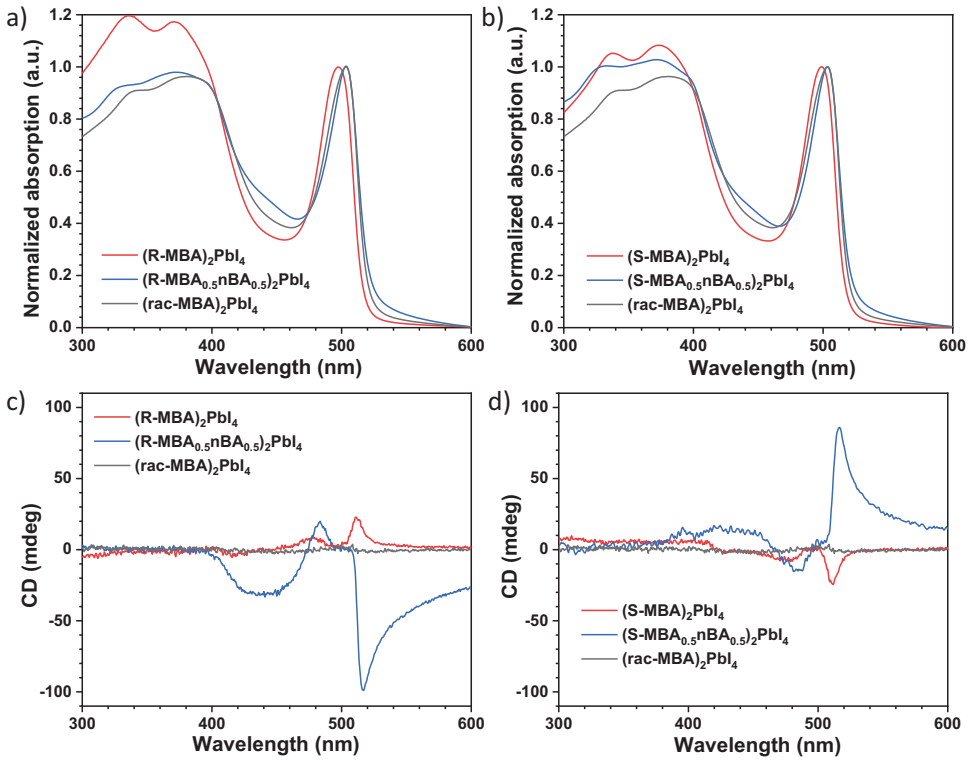

Figure 1. UV–vis absorption and CD spectra. a) Normalized UV–vis absorption spectra and c) CD signals of (R-MBA)$_2$PbI$_4$, (R-MBA$_{0.5}$*n*BA$_{0.5}$)$_2$PbI$_4$, and (rac-MBA)$_2$PbI$_4$ films. b) Normalized UV–vis absorption spectra and d) CD signals of (S-MBA)$_2$PbI$_4$, (S-MBA$_{0.5}$*n*BA$_{0.5}$)$_2$PbI$_4$, and (rac-MBA)$_2$PbI$_4$ films. UV–vis spectra were normalized to the exciton peaks.

2D-CHOIPs enhances the CD signal and modifies its polarity in perovskite lattice structures.

We characterized the morphology and crystal orientation of these films. The top-view scanning electron microscopic (SEM) images reveal that the mixture of organic cations tends to reduce the crystal grain size of (R/S-MBA$_{0.5}$*n*BA$_{0.5}$)$_2$PbI$_4$ as compared with (R/S-MBA)$_2$PbI$_4$ thin films (Figure S2, Supporting Information). The grazing-incidence wide-angle X-ray scattering (GIWAXS) patterns show a slight decrease in preferred crystal orientation after introducing *n*BA$^+$ cations into the (R-MBA$_{0.5}$*n*BA$_{0.5}$)$_2$PbI$_4$ film. However, obvious difference for the (S-MBA$_{0.5}$*n*BA$_{0.5}$)$_2$PbI$_4$ film is observed (Figure S3, Supporting Information). Even though the film morphology and crystal orientation can contribute to CD response due to the linear dichroism and linear birefringence (LDLB) effect,[15] the enhanced CD signals exhibited by the (R/S-MBA$_{0.5}$*n*BA$_{0.5}$)$_2$PbI$_4$ films are mainly due to the enlarged structural distortions to be elaborated below.

2.2. Inorganic Layer Distortions and Asymmetric Hydrogen Bonding Interactions

To understand the change of chiral optical activity upon introducing achiral cations in 2D-CHOIPs, we conducted DFT calculations to quantify their inorganic layer distortions at both intra- and inter-octahedral levels. The DFT calculations were performed with the frozen-core projector augmented-wave (PAW) method[16] implemented in the Vienna Ab initio Simulation Package (VASP) (version 6.2.1)[17] (see Computational Methods in Section 4 for details). The crystal phase and space group symmetry of (R/S-MBA)$_2$PbI$_4$ and (rac-MBA)$_2$PbI$_4$, shown in Table S2 and Figure S4a,b (Supporting Information), agree with previous studies.[2,18] However, for (R/S-MBA$_{0.5}$*n*BA$_{0.5}$)$_2$PbI$_4$, both $P2_12_12_1$ ($Z = 4$) and $P2_1$ ($Z = 2$) phases are found to be likely the ground state crystal structures after structure optimization of various polymorphs. The $P2_12_12_1$ phase is energetically more stable (1.3 meV atom^{-1} lower) than the $P2_1$ phase at $T = 0$ K. Given that a temperature-induced structural transition between $P2_12_12_1$ and $P2_1$ was observed for (R/S-2-MeBA)$_2$PbI$_4$ at ≈180 K[19] and that the $P2_1$ phase was identified for (R/S-MePEA$_{0.5}$*n*BA$_{0.5}$)$_2$PbBr$_4$ by single crystal XRD analysis,[8] we examined the thermodynamic phase stability at finite T by calculating the Gibbs free energies. We find that the $P2_1$ phase becomes thermodynamically more stable at $T > 190$ K (Figure S5, Supporting Information). Moreover, the band gap obtained from the $P2_1$ phase is smaller than that from the $P2_12_12_1$ phase (Figure S6, Supporting Information), which will be discussed later. We thus choose this high-T $P2_1$ phase as the crystal structure for (R/S-MBA$_{0.5}$*n*BA$_{0.5}$)$_2$PbI$_4$ for the rest of the DFT calculations, unless otherwise stated, to better mimic the experimental conditions.

A small but symmetric distortion of the [PbI$_6$]$^{4-}$ octahedra around the inversion center at Pb is observed for (rac-MBA)$_2$PbI$_4$ (Figure S7a, Supporting Information), while (R/S-MBA)$_2$PbI$_4$ and (R/S-MBA$_{0.5}$*n*BA$_{0.5}$)$_2$PbI$_4$ show sizable distortion that breaks the inversion symmetry (**Figure** 2a–d). In (R/S-MBA)$_2$PbI$_4$, the organic cation phenyl rings align approximately

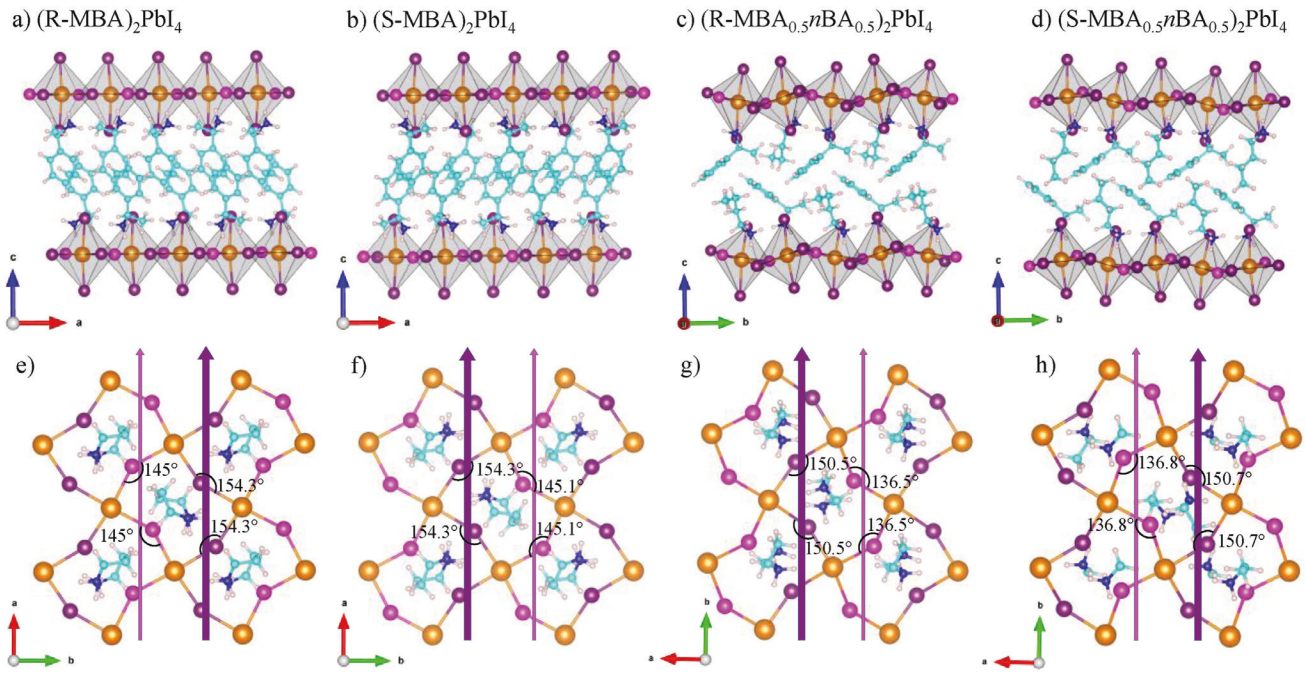

Figure 2. Crystal structural analysis of 2D-CHOIPs. a,e) $(R\text{-}MBA)_2PbI_4$, b,f) $(S\text{-}MBA)_2PbI_4$, c,g) $(R\text{-}MBA_{0.5}nBA_{0.5})_2PbI_4$, and d,h) $(S\text{-}MBA_{0.5}nBA_{0.5})_2PbI_4$. Side (top row) and top (bottom row) view of $[PbI_4]^{2-}$ layers, along with the organic spacer layer containing either pure chiral R/S-MBA^+ cations or mixed chiral R/S-MBA^+ and achiral nBA^+ cations. Color labeling of atoms: Pb (orange); I (purple/pink); C (cyan); H (white); N (blue). Structures are optimized at the DFT level with the D3 van der Waals corrections. The pink and purple axes indicate the screw axes along "a" and "b" directions for $(R/S\text{-}MBA)_2PbI_4$ and $(R/S\text{-}MBA_{0.5}nBA_{0.5})_2PbI_4$, respectively. The larger thickness of the pink arrow indicates larger distortions of the Pb-I-Pb angles from 180°.

parallel to the "*c*" axis (normal to the $[PbI_4]^{2-}$ sheets), while in $(R/S\text{-}MBA_{0.5}nBA_{0.5})_2PbI_4$, the phenyl rings align parallel to the "*a*" axis due to the $CH_3 \cdots \pi$ interactions.[20] To quantitatively describe the octahedral distortion, we examine the bond length distortion index (Δd), bond angle variance (σ^2), and in-plane Pb—I—Pb bond angles. We also measured the hydrogen bond lengths to understand how the mixed chiral–achiral cations impact the octahedral distortions in the inorganic layer.

Both Δd and σ^2 have been used to quantify the intra-octahedral distortion.[3] $(R/S\text{-}MBA_{0.5}nBA_{0.5})_2PbI_4$ exhibits the largest Δd of 0.017 and σ^2 of ≈35 deg^2 in comparison to the values of $(R/S\text{-}MBA)_2PbI_4$ and $(rac\text{-}MBA)_2PbI_4$ (Table S2, Supporting Information), suggesting the largest intra-octahedral distortions. These values are also at the high end compared to those surveyed chiral and achiral cations in 2D perovskites.[5]

The in-plane Pb—I—Pb bond angles reflect the tilting distortions of neighboring octahedra within the inorganic layer (Figure 2e–h and Figure S7b, Supporting Information). Due to the tilting of neighboring octahedra in all four (R, S) compounds, any set of four linked octahedra creates a crinkled square pattern, causing equatorial Pb—I—Pb bond angles to differ drastically from the ideal 180° for an undistorted perovskite sheet (Figure 2e–h). $(R/S\text{-}MBA_{0.5}nBA_{0.5})_2PbI_4$ features similar but more prominent tilting asymmetric distortions than $(R/S\text{-}MBA)_2PbI_4$, with two widely disparate equatorial Pb—I—Pb angles of 150.5° and 136.5°, thus differing by ≈14° compared to ≈9°. The inversion asymmetric inorganic layers are indicated by the different thicknesses of pink and purple arrows. We notice that the pair of $(R\text{-}MBA)_2PbI_4$ and $(S\text{-}MBA_{0.5}nBA_{0.5})_2PbI_4$) have the same order of the distortion (thin, pink vs thick, purple arrows), so do the pair of $(S\text{-}MBA)_2PbI_4$ and $(R\text{-}MBA_{0.5}nBA_{0.5})_2PbI_4$). But the order is opposite between the two pairs (Figure 2e–h), consistent with the flipped CD signals of $(R/S\text{-}MBA_{0.5}nBA_{0.5})$ compared to $(R/S\text{-}MBA)_2PbI_4$. In contrast, $(rac\text{-}MBA)_2PbI_4$ exhibits equal Pb—I—Pb bond angles (150.8°), suggesting that an inversion center is retained (Figure S7b, Supporting Information).

Exploring hydrogen bonding interactions with the in-plane I anions in the inorganic layers provides important insights into the mechanism of the chirality transfer between the organic and inorganic layers. **Figure** 3a,b shows that, in $(R/S\text{-}MBA)_2PbI_4$, each pink-colored I atom interacts with two chiral cations, R- or S-MBA^+, on the opposite sides of the inorganic layer, forming two hydrogen bonds that differ by 0.05 Å. However, each purple-colored I atom does not form hydrogen bonds with chiral cations because the distance between I and H atoms exceeds the van der Waals limit.[21] The slightly asymmetric hydrogen bonding induces the uneven R/S-MBA^+ dependent distortion of in-plane Pb—I—Pb bond angle on the opposite sides of crinkled squares formed by Pb atoms (Figure 2e,f), but that asymmetry does not cause any out-of-plane shift of Pb.[3] In $(R/S\text{-}MBA_{0.5}nBA_{0.5})_2PbI_4$, each pink-colored I atom interacts with one chiral cation, R- or S-MBA^+ on one side of the inorganic layer and one nBA^+ cation on the opposite side of the inorganic layer, forming two more asymmetric and much stronger hydrogen bonds (Figure 3c,d) compared to those in $(R/S\text{-}MBA)_2PbI_4$. The difference between two hydrogen bonds is up to 0.16 Å. Moreover, the hydrogen bond formed between the chiral cation and I (2.48 Å) is much shorter than those (2.81 and 2.86 Å) formed in $(R/S\text{-}MBA)_2PbI_4$.

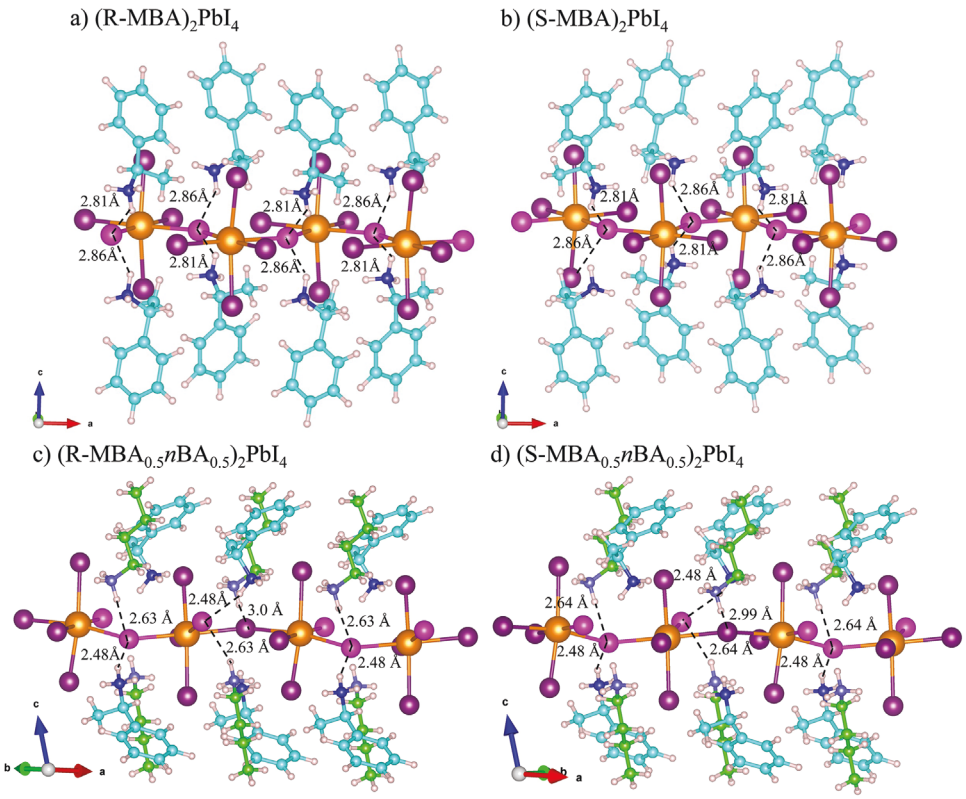

Figure 3. Hydrogen-bonding interactions between the equatorial I anions and organic cations. a) $(R\text{-}MBA)_2PbI_4$, b) $(S\text{-}MBA)_2PbI_4$, c) $(R\text{-}MBA_{0.5}nBA_{0.5})_2PbI_4$, and d) $(S\text{-}MBA_{0.5}nBA_{0.5})_2PbI_4$.

The purple-colored I atoms can form a relatively weak hydrogen bond with nBA$^+$ cation with the bond length of ≈3 Å. The analysis of the hydrogen bonds in $(R/S\text{-}MBA_{0.5}nBA_{0.5})_2PbI_4$ suggests that the incorporation of nBA$^+$ cations results in stronger and more asymmetric hydrogen bonding interaction between the organic cations and inorganic layers.[1] Consequently, a higher degree of asymmetric hydrogen bonds in $(R/S\text{-}MBA_{0.5}nBA_{0.5})_2PbI_4$ leads to larger differences in adjacent equatorial Pb—I—Pb bond angles (Figure 2c,d). Moreover, the alternating arrangement of R/S-MBA$^+$ and nBA$^+$ on both the same and opposite sides of the inorganic layer in $(R/S\text{-}MBA_{0.5}nBA_{0.5})_2PbI_4$ causes an opposite push-and-pull effect of equatorial I atoms, inducing a large angular distortion of the linear Pb—I—Pb bond angle (Figure 3c,d and Figure 2c,d). This out-of-plane distortion contributes to reduced intralayer dimensions and an increased stacking distance, aligning with the XRD structural analysis in this work. In $(rac\text{-}MBA)_2PbI_4$, equal hydrogen bonding interactions are shown on the opposite sides of the inorganic layer (Figure S7c, Supporting Information), which creates equal equatorial Pb—I—Pb bond angles (Figure S7b, Supporting Information) and prevents any out-of-plane shift of Pb atoms (Figure S7c, Supporting Information).

The stronger hydrogen bonding interactions in $(R\text{-}MBA_{0.5}nBA_{0.5})_2PbI_4$ are supported by the Fourier transform infrared (FTIR) spectra (Figure S8, Supporting Information). Furthermore, the steady–state Raman spectra reveal the changes in the ground-state phonon modes in $(R/S\text{-}MBA_{0.5}nBA_{0.5})_2PbI_4$ compared to $(R/S\text{-}MBA)_2PbI_4$ (Figure S9, Supporting Information), supporting the octahedron titling, along with Pb—I—Pb bond angle and Pb—I bond length variations,[22] observed in the corresponding DFT-optimized structures.

2.3. Electronic Band Structures and Spin-Polarized Band-Splitting

To investigate the impact of structural distortions on spin characteristics, we calculated the electronic band structures of 2D-CHOIPs (**Figure 4**) at the HSE06+SOC level.[23] Both $(R/S\text{-}MBA_{0.5}nBA_{0.5})_2PbI_4$ have band gaps smaller by ≈0.07–0.08 eV than their respective $(R/S\text{-}MBA)_2PbI_4$, consistent with the observed red shift of excitonic-peak position in the UV–vis spectra (Figure 1a,b). These results imply that the substitution of chiral R/S-MBA$^+$ cations with achiral nBA$^+$ cations has a noticeable effect on the band gap due to larger distortion of inorganic octahedra, which has been observed in other 2D perovskites.[24]

The overall features of the electronic band structures for $(R/S\text{-}MBA)_2PbI_4$ (Figure 4a,b) are consistent with previous studies.[25] Valence bands (conduction bands), denoted by VB1 and VB2 (CB1 and CB2) in Figure 4, were reported to be spin–split bands resulting from chirality transfer and the SOC effect in the previous studies.[25] However, a closer inspection reveals that each of VB1 and VB2 (CB1 and CB2), in fact, contains two spin-polarized bands, colored red (spin-up), and green (spin-down), with the energy separations less than 4 meV. The splitting of these bands arises from the SOC effects of Pb p orbitals, resulting from the chirality-transfer-driven (i.e., asymmetric hydrogen bonds) inversion symmetry breaking (Figure S10, Supporting Information).

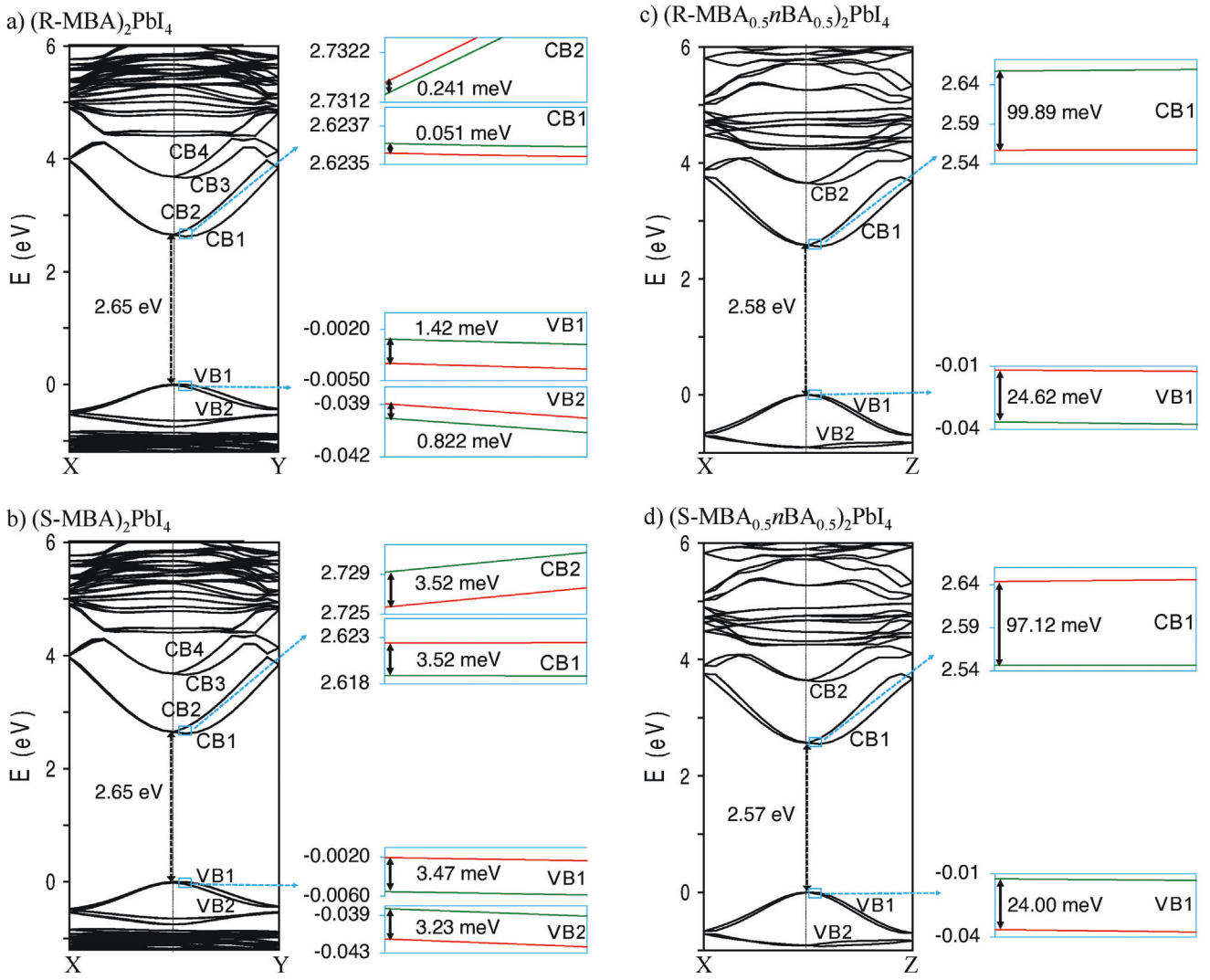

Figure 4. DFT (HSE06+SOC) band structures. a) $(R\text{-}MBA)_2PbI_4$, b) $(S\text{-}MBA)_2PbI_4$, c) $(R\text{-}MBA_{0.5}nBA_{0.5})_2PbI_4$, and d) $(S\text{-}MBA_{0.5}nBA_{0.5})_2PbI_4$, obtained with the 43% exact exchange ($\alpha = 0.43$).[28] The blue rectangle boxes illustrate the zoomed-in view of a segment of the selected (bottom) valence (conduction) bands of near Γ point (at (0.0, 0.056, 0) in the reciprocal lattice coordinates). Red- and green-colored branches indicate the bands with the lifted degeneracy resulted from the inversion symmetry breaking of the octahedra (due to the chirality transfer) and SOC effect. Red (Green): up (down) spin texture of *z*-component of the spin vector. VB (CB): valence (conduction) band. The Fermi level is referenced at $E = 0$ eV.

These results were further verified by using the all-electron code FHI-AIMS[26] with HSE06+SOC.[23] Although the narrow band-splitting in $(R/S\text{-}MBA)_2PbI_4$ was not reported in previous studies,[6b,27] the recent work on $(R/S\text{-}2\text{-}MeBA)_2PbI_4$ shows the same band-splitting features.[19] Without HSE06+SOC, both VB1/VB2 and CB1/CB2, including CB3 and CB4 (third and fourth conduction bands), are nearly twofold degenerated, and the spin-polarized texture of VB1-VB2 and CB1-CB4 is absent (Figure S11a, Supporting Information). For $(rac\text{-}MBA)_2PbI_4$, no such spin-polarized band-splitting is observed, even when the SOC is considered, clearly highlighting the lack of chirality effect on its band structure (Figure S7e, Supporting Information).

In contrast to $(R/S\text{-}MBA)_2PbI_4$, VB1, and CB1 in $(R/S\text{-}MBA_{0.5}nBA_{0.5})_2PbI_4$ comprise two spin-polarized bands along the ΓZ direction (Figure 4c,d). The SOC effect removes the spin-degeneracy of VB1 (CB1), by comparing the band structures without the SOC effect (Figure S11b, Supporting Information). The enhanced spin-polarized band splitting of VB1 (≈24 meV) and CB1 (≈100 meV) originates from the stronger octahedral distortions caused by the asymmetric hydrogen bonds between I atoms and mixed $R/S\text{-}MBA^+$ and nBA^+, as compared to their counterparts containing only $R/S\text{-}MBA^+$ cations. Therefore, the chirality transfer via asymmetric hydrogen bonding is maximized in 2D-CHOIPs with mixed achiral–chiral cations, leading to larger spin-polarized band-splitting. These splits have a stronger effect on conduction bands than valence bands.

The observed CD signals in Figure 1c,d are also likely attributed to the transition of electrons between these Pb/I states, e.g., from Pb(6s) to Pb(6p). We verify this possible permitted transition by calculating the density-of-states of total angular momentum (*j*DOS; $j = l + s$; j = total angular momentum; l = orbital

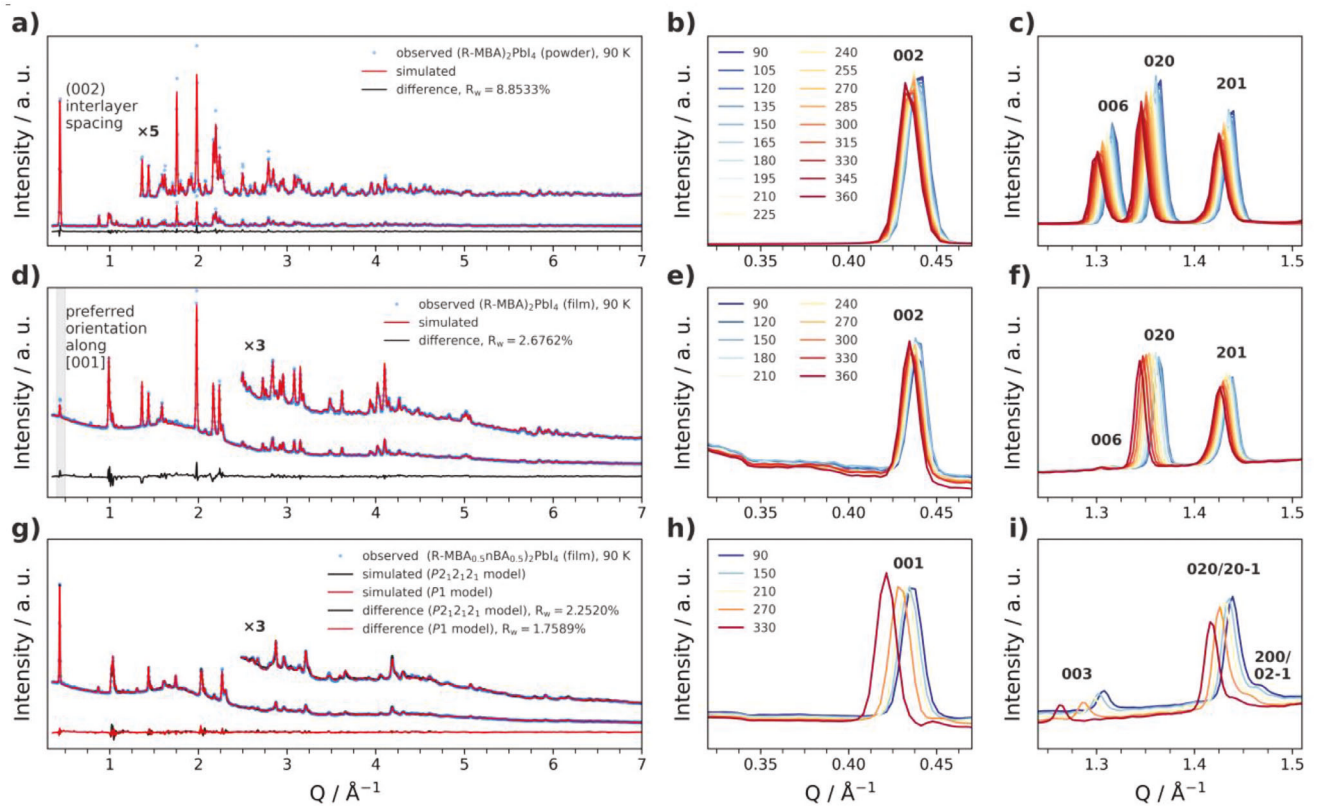

Figure 5. The Rietveld refinement using a two-phase model. a) $(R\text{-}MBA)_2PbI_4$ powder at 90 K and b,c) with peak shifting due to thermal expansion over selected ranges of 2θ. The peak indexing is based on the $P2_12_12_1$ unit cell. d–f) The same for the $(R\text{-}MBA)_2PbI_4$ film sample. g) Rietveld refinement of two possible models using either $P2_12_12_1$ or $P1$ symmetry to the $(R\text{-}MBA_{0.5}nBA_{0.5})_2PbI_4$ at 90 K and h,i) peak shifting due to thermal expansion over selected ranges with peak indexing based on the $P1$ model.

angular momentum; s = spin angular momentum) (Figure S10, Supporting Information). Note that the CD transitions are governed by the electronic transition dipole moment and magnetic transition dipole moment permitted by the selection rules, $\Delta j = 0, \pm 1$. We found that all Pb(6s)- and Pb(6p)-derived valence and conduction bands near the Fermi level correspond to j = ½ (Figure S10, Supporting Information), i.e., $\Delta j = 0$.

2.4. Crystal Structures as a Function of Temperature

The crystal structures of $(R\text{-}MBA)_2PbI_4$ and $(R\text{-}MBA_{0.5}nBA_{0.5})_2PbI_4$ were further investigated using temperature-dependent powder X-ray diffraction (PXRD) and pair distribution function (PDF) analysis. The PXRD patterns at 90 K and respective Rietveld refinements for $(R\text{-}MBA)_2PbI_4$ powder and film samples and $(R\text{-}MBA_{0.5}nBA_{0.5})_2PbI_4$ film are shown in **Figure** 5a,d,g, respectively. The shifting of Bragg reflections due to thermal expansion for all three samples over selected ranges of 2θ is observed (Figure 5). A more detailed discussion of Rietveld refinements is reported in a separate paper.[10] The first diffraction peak at $Q \approx 0.43$ Å^{-1} (where $Q = 2\pi/d_{hkl}$) for all samples corresponds to interlayer spacing of ≈14.6 Å. With increasing temperature from 90 K to around 300 K, a continuous peak shifting was observed without any indication of phase transitions.

The trends in a, b, interlayer distance, and volume per layer are compared for the three samples in **Figure** 6. The diffraction pattern measured from the $(R\text{-}MBA)_2PbI_4$ film was different from that measured by the signal crystal flakes in capillary geometry which has been reported by our previous work.[10] There are clear systematic (near)absences of the 00l reflections in the film sample geometry. This suggests that the film has preferred orientation along the stacking direction [00l], which can be expected to reduce intensities in the 00l and hkl peaks, while hk0 peaks remain strong. To further test this, the March-Dollase model[29] was used as implanted in TOPAS v6 to correct for the preferred orientation effects. This led to a reasonably good description of the diffraction pattern from the $(R\text{-}MBA)_2PbI_4$ in film-transmission geometry, as shown in Figure 5, confirming the use of the same structure model as for the capillary samples. A good agreement in the results is obtained for the $(R\text{-}MBA)_2PbI_4$ powder and film samples, suggesting that the sample geometry does not have a substantial impact on the thermal expansion, and that the preferred orientation does not hinder us from obtaining reliable values. Regardless of the model used, the refinements suggest that the addition of nBA$^+$ cations has a large effect on the unit cell dimensions. There is a significant contraction in both a and b, which become more isotropic. Although further confirmation is needed, these findings align with the trends in the thermal expansion of lattice parameters and volume for the published structures with nBA$^+$ and MeBA$^+$ rather than MBA$^+$ as the organic

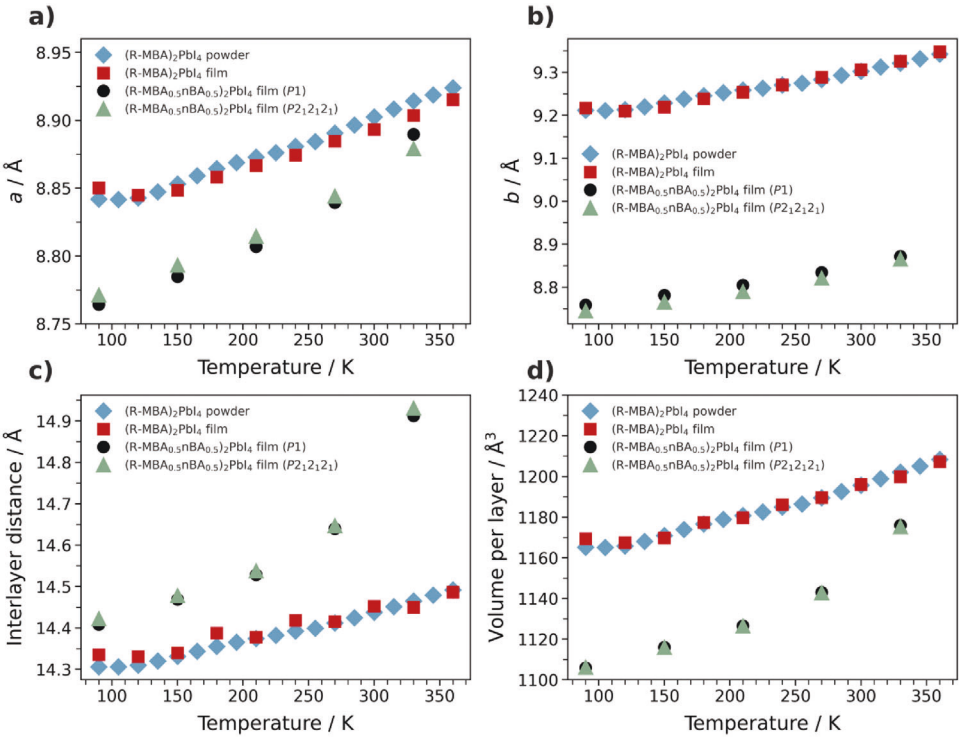

Figure 6. Trends of the unit cell parameters as a function of temperature. a) *a*, b) *b*, c) interlayer spacing, and d) volume per layer for the different samples.

molecule.[9] These observations are consistent with the XRD results (Figure S1, Supporting Information) and the DFT calculations (Table S2, Supporting Information). Based on the DFT calculations, the mixture of two different organic components could cause stronger but asymmetric hydrogen bonding in (R/S-$MBA_{0.5}nBA_{0.5})_2PbI_4$, leading to more isotropic (on-average) intralayer dimensions, while larger out-of-plane octahedral distortions could lead to reduced intralayer dimensions and an increased stacking distance.

PDF measurements take the diffuse scattering into account in addition to the Bragg reflections to generate a pair distribution function $G(r)$, which gives a weighted probability of finding two atoms separated by a distance r. A major advantage of PDF measurements is that they allow the local structure to be analyzed separately from the long-range average structure.[30] Temperature-dependent X-ray total scattering measurements and PDF analysis were obtained using PDFgetX3[31] to characterize the local structures of $(R\text{-}MBA)_2PbI_4$ and $(R\text{-}MBA_{0.5}nBA_{0.5})_2PbI_4$ (**Figure 7**). While methods for analyzing PDF data from textured samples are being actively developed,[32] we only analyzed the powdered samples for $(R\text{-}MBA)_2PbI_4$ to avoid this issue. The published chiral structure was used as a starting point to model the local structure signal.[2] The R/S-MBA^+ cations contribute little to the total signal, because the x-ray scattering power is significantly weaker

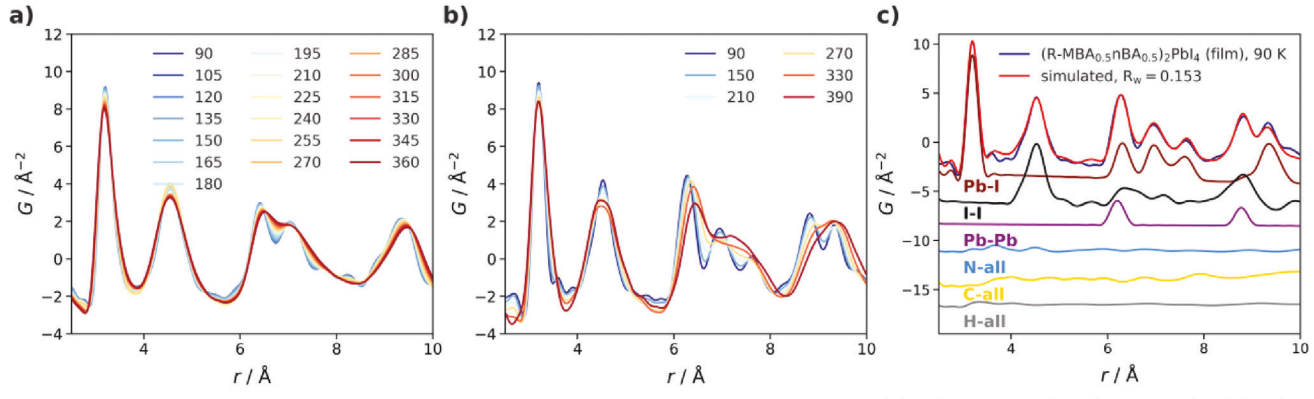

Figure 7. Comparison of temperature-dependent PDFs. a) $(R\text{-}MBA)_2PbI_4$ and b) $(R\text{-}MBA_{0.5}nBA_{0.5})_2PbI_4$ plotted from lowest temperature (blue) to highest temperature (red). c) The partial contributions to the total PDF are compared as calculated from the model refined to the data measured at 90 K.

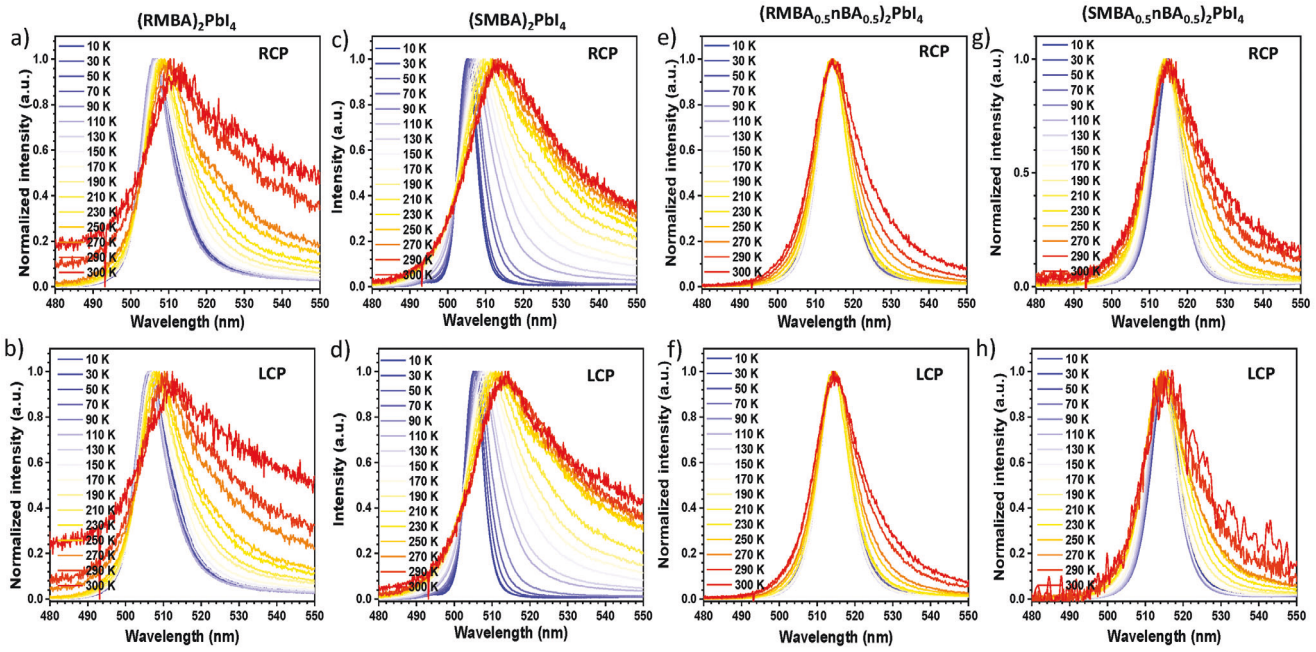

Figure 8. Temperature-dependent circular polarized photoluminescence (CPPL). Normalized CPPL of a) RCP and b) LCP of (R-MBA)$_2$PbI$_4$, c) RCP and d) LCP of (S-MBA)$_2$PbI$_4$, e) RCP and f) LCP of (R-MBA$_{0.5}$*n*BA$_{0.5}$)$_2$PbI$_4$, and g) RCP and h) LCP of (S-MBA$_{0.5}$*n*BA$_{0.5}$)$_2$PbI$_4$ thin films taken at the heating-up process from 10 to 315 K. The PL emission was detected at the right and left circular polarized mode by setting the polarizer at 315° and 45°, respectively.

for the organic component due to the lower number of electrons on these atoms. For this reason, we neglected modeling of any specific structural modifications to the organic sub-structure as a function of temperature or chirality.

The first large peak at a distance of ≈3.2 Å can be indexed solely to neighboring Pb–I pair distances. The second large peak at ≈4.55 Å comes from I–I pairs. The Pb–Pb pair distance is at 6.4 Å and farther Pb–I pairs are at 7.1 and 9.4 Å. In comparison to the experimental data, the DFT structures show significantly contracted atom-pair distances, as summarized in Table S3 (Supporting Information), which may be partially due to the absence of thermally activated dynamics. Nevertheless, both DFT and PDF determined structures show a slight contraction of atom-pair distances for (R-MBA$_{0.5}$*n*BA$_{0.5}$)$_2$PbI$_4$ versus (R-MBA)$_2$PbI$_4$, which correlates with the smaller unit cell volume. From the DFT calculations, this is ascribed to stronger hydrogen bonding interactions and push-and-pull of alternative I atoms in the adjacent octahedra, resulting in increased buckling of Pb—I—Pb bond and shortening of Pb–Pb distance. Interestingly, the local structure of (R-MBA$_{0.5}$*n*BA$_{0.5}$)$_2$PbI$_4$ shows narrower peak-widths than for (R-MBA)$_2$PbI$_4$ sample at lower temperatures, suggesting a more ordered arrangement of the inorganic layers.

Comparison of temperature-dependent PDFs for (R-MBA)$_2$PbI$_4$ and (R-MBA$_{0.5}$*n*BA$_{0.5}$)$_2$PbI$_4$ are plotted in Figure 7c. Qualitatively, at low temperatures, the Pb–I and I–I pair distributions are sharper, indicating a smaller spread of values. The changes observed on increasing temperature are more drastic, and at high temperatures, the PDF of the (R-MBA$_{0.5}$*n*BA$_{0.5}$)$_2$PbI$_4$ sample shows broader peaks beyond ≈6.5 Å due to stronger octahedral distortions. The trends in the nearest neighbor Pb–Pb distances with the increase of temperature are given in Figure S13 (Supporting Information) for both (R-MBA)$_2$PbI$_4$ and (R-MBA$_{0.5}$*n*BA$_{0.5}$)$_2$PbI$_4$. The trends show an on-average shorter magnitude for (R-MBA$_{0.5}$*n*BA$_{0.5}$)$_2$PbI$_4$ but a higher thermal expansion value in conjunction with the larger crystallographic thermal expansion. The second nearest neighbors are also contracted and closer in value (not shown), as might be expected for the shorter, more isotropic in-plane lattice parameters.

2.5. Circularly Polarized and Time-Resolved Photoluminescence as a Function of Temperature

To investigate the impact of achiral–chiral cations induced strong structural distortions and asymmetric thermal expansion on chiroptoelectronic activity of (R/S-MBA$_{0.5}$*n*BA$_{0.5}$)$_2$PbI$_4$, we measured the temperature-dependent circularly polarized photoluminescence (CPPL) of the (R/S-MBA)$_2$PbI$_4$ and (R/S-MBA$_{0.5}$*n*BA$_{0.5}$)$_2$PbI$_4$ thin films (**Figure 8**). The PL emission was detected at the right and left circularly polarized mode (RCP and LCP) for each film. In order to quantify the degree of the difference of CPPL for 2D-CHOIPs, we calculated the degree of photoluminescence polarization (DP) by: $P = \frac{I_{left} - I_{right}}{I_{left} + I_{right}}$, where I_{left} and I_{right} are the emission intensities at LCP and RCP mode, respectively.[12] For both (R/S-MBA)$_2$PbI$_4$ thin films, the *P*% values are below 0.1 without any clear trend along the variation of temperature (Figure S14a, Supporting Information). The exfoliated single crystal samples, however, show increased *P*% values with decreasing temperature.[12] This might be attributed to the polycrystalline and multilayer stacking features of thin film samples, which bring additional traps and reduce the difference between the emissions of LCP and RCP light. However, as shown in Figure S14b (Supporting Information), the addition of achiral cations in (R/S-MBA$_{0.5}$*n*BA$_{0.5}$)$_2$PbI$_4$ thin films leads

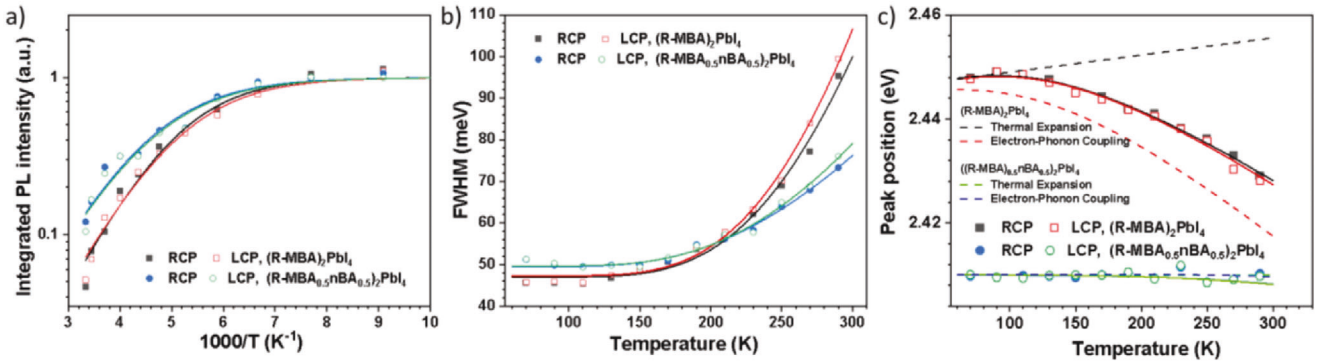

Figure 9. Temperature-dependent CPPL characteristics at the RCP and LCP mode. a) Integrated PL intensity as a function of the reciprocal temperature, b,c) The FWHM of PL peak and the PL peak energy versus temperature, respectively, of the $(R\text{-}MBA)_2PbI_4$ and $(R\text{-}MBA_{0.5}nBA_{0.5})_2PbI_4$ thin films. The solid lines represent the fitting results.

to a significant increase in the *P*% values to ≈2.5 over a wide range of test temperatures. The results suggest that the chirality transfer is more efficient when achiral cations are included in the organic layer.

The CPPL spectra of $(R/S\text{-}MBA)_2PbI_4$ films show a clear redshift and significant asymmetric peak broadening at both RCP and LCP PL emissions with increasing temperature (Figure 8a–d). In stark contrast, the $(R/S\text{-}MBA_{0.5}nBA_{0.5})_2PbI_4$ films show no peak shift, and only slight asymmetric peak broadening is observed with the increase in temperature (Figure 8e–g). To further understand how the addition of achiral cations into the organic layers affects the chiroptoelectronic activity, we fitted experimental CPPL characteristics with theories to gain exciton binding energy, electron–phonon coupling strength, and the effect of thermal expansion and electron–phonon coupling on the band structures. We fitted the integrated PL intensity as a function of the reciprocal temperature with the Arrhenius equation to extract the exciton binding energy[33]:

$$I(T) = \frac{I_0}{1 + aT^{\frac{3}{2}} \exp\left(\frac{-E_b}{k_B T}\right)} \quad (1)$$

where $I(T)$ is the normalized integrated PL intensity at a given temperature T, a is constant, k_B is the Boltzmann constant, E_b is the exciton binding energy, and I_0 is the PL intensity at low-temperature limit (0 K), respectively. The integrated wavelength range was from 476 to 563 nm. The fitted results are shown in **Figure 9a**. There is no obvious difference between the RCP and LCP mode for each sample, but they exhibit different trends with the increase of temperature, which implies the difference in their exciton binding energies (Table S4, Supporting Information). Slightly lower E_b (≈89 meV vs 91 meV) for $(R\text{-}MBA_{0.5}nBA_{0.5})_2PbI_4$ suggests partially replacing chiral aryl R/S-MBA^+ with achiral alkyl nBA^+ can alter the exciton binding energy due to the dielectric confinement effect.[34] In addition, the smaller exciton binding energies compared to those reported for 2D perovskites[35] suggest that the model in use may not fully capture the nuances of 2D systems, where additional considerations such as the reduced dimensionality and dielectric confinement are crucial. Indeed, PL spectra alone may not provide a complete picture of exciton binding energy, especially in 2D systems, as other factors (e.g., exciton–phonon interactions and dielectric environment) could also play a significant role.

The Gauss-Lorentz fitted temperature-dependent CPPL full width at half maximum (FWHMs) are presented in Figure 9b. From which, we can investigate the charge carrier-phonon coupling strength that has been attributed to the inorganic lead halide octahedron motions.[36] The FWHM of $(R\text{-}MBA)_2PbI_4$ increases from 40 to 100 meV with the temperature increased from 10 to 300 K. This more than twofold broadening of the emission peak implies a strong charge carrier-phonon coupling. In contrast, the FWHM of $(R\text{-}MBA_{0.5}nBA_{0.5})_2PbI_4$ just increases from 50 to 70 meV in the same temperature range. The smaller broadening of the peak indicates the reduced phonon coupling and carrier scattering in $(R\text{-}MBA_{0.5}nBA_{0.5})_2PbI_4$ perovskites.[33] The evolution of FWHM of the emission peaks can take into account the coupling of the charge carrier to the acoustic phonons as well as the longitudinal optical (LO) phonons described by Fröhlich Hamiltonian:[37]

$$\mathrm{FWHM}\%\%(T) = \Gamma_0\% + \Gamma_{ac}T + \frac{\Gamma_{homo}}{e^{\hbar\omega_{homo}/K_B T} - 1} \quad (2)$$

$$\Gamma_{homo} = \frac{\hbar M \omega_{homo}}{\rho L}\% \left(\frac{D}{\hbar\omega_{homo}}\right)^2 \left(2 - e^{-\frac{\hbar\omega_{homo}}{K_B T}}\right) \quad (3)$$

where Γ_0 is the inhomogeneous linewidth at 0 K due to structural disorder, Γ_{ac} is the acoustic-phonon and exciton coupling term, Γ_{homo} is the LO-phonon and exciton coupling term, ω_{homo} is the homopolar phonon angular frequency, $\hbar\omega_{homo}$ is the energy of the LO-phonon, M is the sum of electron and hole effective masses, ρ is the mass density, L is the thickness of the quantum well where the exciton is confined, and D is the deformation potential of the band gap induced by the homopolar phonons. The effective masses of electron and hole are $0.78m_0$ and $0.94m_0$ for $(R\text{-}MBA)_2PbI_4$ and $0.95m_0$ and $0.76m_0$ for $(R\text{-}MBA_{0.5}nBA_{0.5})_2PbI_4$, extracted from our DFT calculations (Figure S15, Supporting Information), where m_0 is the electron rest mass. The ω_{homo} for the Pb–I–Pb stretch, the density (ρ), and the width of the quantum well (L) are 98.8 cm^{-1}, 2.804×10^{-3} kg cm^{-3}, and 0.61 nm, respectively.[10] The extracted values of Γ_0, Γ_{ac}, $\hbar\omega_{homo}$, and D are summarized in Table S4 (Supporting Information). The values of Γ_0 for $(R\text{-}MBA_{0.5}nBA_{0.5})_2PbI_4$ at the RCP and LCP mode

are about 3 meV larger than those for (R-MBA)$_2$PbI$_4$, implying a larger structural disorder, which is consistent with the larger octahedral distortions obtained in our DFT calculations. The values of Γ_{ac} for (R-MBA$_{0.5}$*n*BA$_{0.5}$)$_2$PbI$_4$ at the RCP and LCP mode are around 0.4 meV K^{-1}, significantly smaller than those of ≈1.7 meV K^{-1} for (R-MBA)$_2$PbI$_4$. The weaker acoustic-phonon and exciton coupling could be due to the stronger hydrogen bonding interactions that enhances the rigidity of the inorganic frameworks in (R-MBA$_{0.5}$*n*BA$_{0.5}$)$_2$PbI$_4$. A small charge carrier LO-phonon coupling typically would reduce the scattering during charge transport and increase the carrier mobility of the film. Subsequently, this will result in an augmented carrier injection and transport efficiency. The D value of (R-MBA$_{0.5}$*n*BA$_{0.5}$)$_2$PbI$_4$ is about three times smaller than that of (R-MBA)$_2$PbI$_4$, further indicating the weaker electron-phonon coupling with the addition of *n*BA$^+$ cations in 2D-CHOIPs. The reduced electron–phonon coupling in the (R-MBA$_{0.5}$*n*BA$_{0.5}$)$_2$PbI$_4$ might arise from the distortion of the inorganic layer, introduced by the reduced π–π interactions of chiral R/S-MBA$^+$ cations by *n*BA$^+$ substitution.

Further analysis of the peak position variation with temperature is presented in Figure 9c. The temperature-dependent changes in the emission peak are primarily governed by thermal expansion (TE) and electron-phonon (EP) coupling.[38] In addition to the change in the band structure caused by thermal expansion, the electron–phonon coupling can also have a significant impact on the band structure at different temperatures.[38b] With the one-oscillator model, the following equation is used to quantify the effects of TE and EP coupling on the band gap variation with temperature:[9]

$$E_g(T) = E_0 + A_{TE}T + A_{EP}\left[\frac{2}{e^{(\hbar\omega/K_B T)} - 1} + 1\right] \quad (4)$$

where E_0 is the unrenormalized bandgap, A_{TE} and A_{EP} are the weight of the TE and EP coupling, respectively, and $\hbar\omega$ is the average optical phonon energy contributing to EP coupling. The fitting results are in Table S4 (Supporting Information). A similar trend of EP coupling was also obtained as fitted from FWHM. It is worth mentioning that the obtained A_{TE} value for (R-MBA$_{0.5}$*n*BA$_{0.5}$)$_2$PbI$_4$ is much smaller than that of (R-MBA)$_2$PbI$_4$, which indicates suppressed lattice expansion, especially in the "*b*" direction as shown in Figure 6b.

We also collected temperature-dependent time-resolved PL spectra and used them to further explore the electron–phonon scattering in (R/S-MBA)$_2$PbI$_4$ and (R/S-MBA$_{0.5}$*n*BA$_{0.5}$)$_2$PbI$_4$ thin films (Figure S16, Supporting Information). The PL decay process ramps up as the temperature increases from 10 to 300 K for all the four films. The decay process was fitted by two exponential components ($I(t) = A_1 e^{-\frac{t}{\tau_1}} + A_2 e^{-\frac{t}{\tau_2}}$) and plotted in Figure S17 (Supporting Information). A power law dependence of scattering rate T^γ was observed, which is also expected for electron–phonon scattering.[39] $\gamma > 0$ indicates that phonons are the main sources of scattering, while $\gamma < 0$ indicates that charge impurities are the main sources of scattering. Scattering by acoustic phonons will lead to $\gamma = 1$, while $\gamma > 1$ suggests that optical phonons are included in the scattering process.[40] In Figure S17a (Supporting Information), (R-MBA)$_2$PbI$_4$ shows positive γ values over the test temperature, indicating phonons contribute to the scattering, which agrees with the results obtained from the temperature-dependent CPPL measurements. Even though the γ values at low temperatures (10 to ≈150 K) are much smaller than 1, it is difficult to identify whether acoustic phonons contribute to the scattering. However, there is no doubt that the optical phonons contribute to the scattering at high temperatures (≈150–300 K), given by the γ values of 3.91 and 2.73. For the (R-MBA$_{0.5}$*n*BA$_{0.5}$)$_2$PbI$_4$ thin film (Figure S17b, Supporting Information), γ values are negative at low temperatures, suggesting the existence of charge impurities. This indicates different exciton formation and relaxation. At the high-temperature region (≈120–300 K), the γ values are much larger than 1, suggesting the optical phonon contributes to the scattering.[41] Nonetheless, the temperature-dependent PL dynamics also show different phonon scattering behaviors for (R/S-MBA)$_2$PbI$_4$ and (R/S-MBA$_{0.5}$*n*BA$_{0.5}$)$_2$PbI$_4$ films.

Femtosecond transient absorption (*fs*-TA) spectroscopy can provide information on hot-carrier cooling, which involves the electron–phonon interactions at the excited states. Therefore, we conducted the *fs*-TA spectroscopic measurements at different excitation fluences. Figure S18a,b (Supporting Information) shows the normalized TA spectra at an excitation of 3.54 eV (350 nm) for (R-MBA)$_2$PbI$_4$ and (R-MBA$_{0.5}$*n*BA$_{0.5}$)$_2$PbI$_4$. As the delay time increases, the photobleaching and photoinduced absorption bands red shifts for (R-MBA)$_2$PbI$_4$, while they remain almost unchanged for (R-MBA$_{0.5}$*n*BA$_{0.5}$)$_2$PbI$_4$. The hot carrier temperature (T_c) evolutions at two pump fluences show the initial hot-carrier cooling in (R-MBA)$_2$PbI$_4$ is dominated within the sub-picosecond time scale (<1 ps), while an additional slow cooling process is observed on a timescale of up to hundreds (Figure S18c, Supporting Information), which is attributed to the hot-phonon bottleneck effect.[42] However, hot-carrier cooling in (R-MBA$_{0.5}$*n*BA$_{0.5}$)$_2$PbI$_4$ shows a similar cooling rate over the timescale from sub-picosecond to hundreds picosecond, indicating different carrier–phonon interactions after the introduction of achiral *n*BA$^+$ cations as discussed for the temperature-dependent CPPL and time-resolved PL studies.

3. Conclusion

Mixing chiral R/S-MBA$^+$ and achiral *n*BA$^+$ cations in the organic spacer layer is used as an effective method to manipulate the structural and chiroptoelectronic activity of 2D-CHOIP (R/S-MBA$_{1-x}$*n*BA$_x$)$_2$PbI$_4$. Flipped and enlarged circular dichroism signals are observed in (R/S-MBA$_{0.5}$nBA$_{0.5}$)$_2$PbI$_4$. DFT calculations reveal the enhanced asymmetric hydrogen bonding interactions between the organic and inorganic layers in the mixed chiral–achiral 2D-CHOIPs, which causes more distorted inorganic layers at both the intra- and inter-octahedral levels, increases the chirality transfer, and enlarges spin-polarized band-splitting. Temperature-dependent powder XRD and PDF structure studies show the compressed intralayer lattice, enlarged interlayer spacing, and more organized local structures. Temperature-dependent CPPL and time-resolved PL as well as femtosecond transient absorption spectroscopic studies indicate that the electron–phonon coupling plays an increasing role in emission and hot electron decay dynamics. The unchanged PL peak position and slightly asymmetric peak broadening with increasing temperature suggest the potential application of these

2D-CHOIPs for promising color-stable circularly polarized light-emitting diode devices. Our results open a gateway to manipulate the chiroptoelectronic activity in 2D-CHOIPs, provide an in-depth understanding of the structure-property relationship, and demonstrate their potential for temperature-insensitive device applications.

4. Experimental Section

Materials: Lead (II) iodide (PbI_2, 99.99%), *N*,*N*-Dimethylformamide (DMF, anhydrous, ≥99.8%), diethyl ether (≥99%), *N*,*N*-dimethyl sulfoxide (DMSO, anhydrous, ≥99.9%), ethanol (≥99.5%), hydroiodic acid (57 wt% stabilized with 1.5% hypophosphorous acid), organic amine (±)-α-methylbenzylamine (rac-MBA, >98%), (R)-(+)-α-methylbenzylamine (R-MBA, >98%), and (S)-(−)-α-methylbenzylamine (S-MBA, >98%) were purchased from Sigma-Aldrich (St. Louis, Missouri) without further purification. *n*-Butylammonium iodide (*n*BAI) was purchased from GreatCell Solar (Queanbeyan, Australia) without further purification.

Synthesis of Rac-MBAI, R-MBAI, and S-MBAI: Rac-MBAI was synthesized by dissolving (±)-α-methylbenzylamine (5 mL) in 30 mL of ethanol in an ice bath. Hydroiodic acid aqueous solution (5.8 mL) was added dropwise to the flask with vigorous stirring. After the addition of hydroiodic acid, the mixture was allowed to stand in an ice bath for another 20 min until a colorless precipitate appeared. The precipitate was filtered under vacuum and washed thoroughly using cold diethyl ether. The crude precipitate was collected and recrystallized in ethanol twice to obtain thin, granular-like white crystals. R-MBAI and S-MBAI were synthesized following the same procedure but simply replacing (±)-α-methylbenzylamine to (R)-(+)-α-methylbenzylamine or (S)-(−)-α-methylbenzylamine (5 mL).

Fabrication of 2D Chiral Perovskite Thin Films: Plain glass substrates (Fisher Scientific) were cut into a size of 15 mm × 15 mm and cleaned followed the procedure reported before.[10] For pure (rac-MBA)$_2$PbI$_4$, (R-MBA)$_2$PbI$_4$, and (S-MBA)$_2$PbI$_4$ perovskite thin films, a 20 wt% perovskite precursor composed rac-MBAI (0.8 mM) and PbI_2 (0.4 mM) were added in a 1 mL mixed solvent (972 µL DMF and 28 µL DMSO) and stirred at 70 °C for 1–2 h. Perovskite films of (R-MBA$_{1-x}$*n*BA$_x$)$_2$PbI$_4$ and (S-MBA$_{1-x}$*n*BA$_x$)$_2$PbI$_4$ with x = 0, 0.1, 0.3, 0.5, 0.7, 0.9, and 1.0 were made by replacing R-MBAI or S-MBAI with *n*BAI. The precursor was filtered with a 0.22 µm PTFE filter before spin coating. A 2D chiral perovskite film was fabricated by spin coating a 30 µL precursor solution at 2000 rpm for 30 s followed by annealing at 100 °C for 10 min.

Characterization of 2D Chiral Perovskite Films: Scanning electron microscopic (SEM), X-ray diffraction (XRD), Ultraviolet–visible (UV–vis) absorption spectra, Fourier transform infrared spectroscopy (FTIR) were conducted on Cornell Center for Materials Research Shared Facilities with the conditions in the previous publication.[43] Raman spectra were collected using a WITec alpha300R confocal Raman microscope. Steady-state photoluminescence (PL) measurements of spin-casted thin films on quartz substrates were captured using an Edinburgh FLS1000 Spectrometer with an excitation wavelength of 410 nm and a long pass filter of 490 nm wavelength. The transmission circular dichroism (CD) data of spin-casted thin films were collected using a CD spectrometer (J-1500, JASCO).

The grazing-incidence wide-angle X-ray scattering (GIWAXS) measurements were conducted at the Complex Materials Scattering (CMS, 11-BM) beamline of the National Synchrotron Light Source II (NSLS-II) at the Brookhaven National Laboratory (BNL) with the conditions in the previous publication.[43] Broadband pump–probe transient absorption (TA) spectroscopy[43] and temperature-dependent circularly polarized photoluminescence (CPPL)[10] measurements were performed at the BNL Center for Functional Nanomaterials (CFN).

Time-resolved PL decays were measured with the same microscope by using the time-correlated single photon counting method. A single photon counting avalanche (COUNT 50C from Laser Components) in combination with a time analyzer (PicoHarp 300, Picoquant Germany) was used to record time-resolved PL signals. PL decays were individually fit with the Fluofit (Picoquant) software using an exponent model.

Temperature-dependent powder X-ray diffraction (PXRD) and pair distribution function (PDF) measurements were performed on xPDFsuite. X-ray total scattering measurements were conducted using beamline 28-ID-2 of NSLS-II at BNL. The details for data collection and analysis can be found in the previous publication.[10]

Rietveld Refinements: Rietveld refinements can be found in the previous publication.[10] The same basic fitting setup was used to generate reasonable structure models for extracting the trends of the lattice parameters for the mixed cation film sample. Both the $P2_12_12_1$ and a *P1* model with only one layer per unit cell were set up with half the R-MBA molecules replaced with *n*BA. Then, the structures were refined to obtain the best fit. For all three samples ((R-MBA)$_2$PbI$_4$ powder, (R-MBA)$_2$PbI$_4$ film(R-MBA$_{0.5}$*n*BA$_{0.5}$)$_2$PbI$_4$), the temperature-dependent lattice parameters were tracked by iterative refinement from low to high temperature.

PDF Refinements: PDF refinements were done follow the same method in the previous publication.[10] The same model was used for the mixed cation sample, assuming that it gives a suitable model of the local intralayer structure in both cases.

Computational Methods: The structure optimization was performed using the generalized gradient approximation (GGA) of exchange–correlation functional with the Perdew–Burke–Ernzerhof (PBE)[44] parameterization plus the DFT-D3 method[45] with Becke–Jonson damping to incorporate the van der Waals (vdW) dispersion interaction. The hybrid HSE06 functional[23] with spin–orbit coupling (SOC), with 43% exact exchange (α = 0.43),[27] was employed to obtain a more accurate description of the band gap and capture the relativistic effect introduced by heavy atom Pb in the systems. For the DFT-HSE06+SOC band structure calculations, all the geometries relaxed at the DFT-vdW level were used, and no vdW correction was applied. All structures were relaxed without any symmetry constraint until the force on each of the ions was 0.01 eV Å^{-1} or less. A plane-wave basis set with an energy cutoff of 400 eV was used. The Monkhorst–Pack[46] k-point sampling was utilized for the Brillouin zone integration. To speed up the calculation, all DFT-HSE06+SOC calculations were performed with the GPU version of VASP 6.2.1. The Visualization for Electronic and Structural Analysis (VESTA)[47] software was used to render the crystal structures. The symmetries of all optimized structures were obtained using FINDSYM.[48] The AFLOW notations of the high-symmetry points in the Brillouin zone[49] were adopted for the band structure calculations.

(R/S-MBA)$_2$PbI$_4$: The initial structures were obtained from the literature and database.[2,3,50] Among those, the structures taken from the report[2] had the lowest energies at the PBE-D3 level. A k-mesh of 9 × 9 × 3 was used for energy calculation. The interplanar distances (*d*-spacing) and lattice parameters of the optimized structures are presented in Table S1 and S2 (Supporting Information), respectively. The optimized structures are displayed in Figure 2a,b,e,f.

(rac-MBA)$_2$PbI$_4$: Like (R/S-MBA)$_2$PbI$_4$, the initial structure of (rac-MBA)$_2$PbI$_4$ was also obtained from the literature.[51] Additionally, multiple candidate structures differing in both symmetry and formula unit (*Z*) were generated by modification of the existing structure of (R/S-NEA)$_2$PbBr$_4$[2,7c] and (R/S-MBA)$_2$SnI$_4$[8] following the reports.[52] In those structures, Br and Sn were replaced with I and Pb, respectively; NEA was modified to form MBA. After DFT-D3 optimization, with a 5 × 9 × 9 k-mesh, the structure derived from the report[51b] was determined as the lowest energy structure. The *d*-spacing and lattice parameters of the optimized structures are presented in Tables S1 and S2 (Supporting Information), respectively. The optimized structures are displayed in Figure S7a,b (Supporting Information).

(R/S-MBA$_{0.5}$*n*BA$_{0.5}$)$_2$PbI$_4$: Because there is no reported structure of (R/S-MBA$_{0.5}$*n*BA$_{0.5}$)$_2$PbI$_4$, multiple candidate structures of these systems were generated from similar existing structures. These are (R/S-MePEAC4)$_2$PbBr$_4$ (space group: $P2_1$; Z = 2),[8] (R/S-MBA)$_2$PbI$_4$ (space group: $P2_12_12_1$, Z = 4),[2,3] and the structures (with *P1*, $P2_1$, and $P2_12_12_1$ symmetries) from the Rietveld refinements of PDF/XRD data of (R/S-MBA$_{0.5}$*n*BA$_{0.5}$)$_2$PbI$_4$ at 90 K (Figures 5–7) following the previous work.[52b,c,d,53] Two approaches were taken. In the first approach, the

motif structures of (R/S-MBA$_{0.5}n$BA$_{0.5}$)$_2$PbI$_4$ were obtained from (R/S-MePEAC4)$_2$PbBr$_4$, where all MePEA cations were converted to MBA by removing the extra –CH$_2$– and replacing the Br$^-$ anions with I$^-$ anions. In the second approach, the motif structures of (R/S-MBA$_{0.5}n$BA$_{0.5}$)$_2$PbI$_4$ were generated from (R/S-MBA)$_2$PbI$_4$ by replacing half of the R/S-MBA$^+$ cations with the same number of nBA$^+$ cations in every alternating layer.

The low-T structure was obtained (Figure S4d, Supporting Information) from the temperature dependent PDF analysis and the high-T structure (Figure S4c, Supporting Information) from the DFT calculation. The DFT energies were calculated (at $T = 0$ K) for both structures, and it was found that the orthorhombic structure (Figure S4d, Supporting Information) is the lowest energy structure, i.e., the most stable at $T = 0$ K. So, the orthorhombic structure (Figure S4d, Supporting Information) was called as the low-T structure. However, when the phase stability was calculated at finite T (Figure S5, Supporting Information), the monoclinic phase (Figure S4c, Supporting Information) was found to be more stable at $T = 200$ K (see Gibbs free energy, G, for the monoclinic phase (blue curve) is more negative in Figure S5, Supporting Information). For this reason, the monoclinic phase was called (Figure S4c, Supporting Information) as the high-T phase.

Non-colinear SOC total angular momentum (j) calculation: To obtain j for different non-colinear SOC bands, it is necessary to carry out full relativistic DFT calculation, which is not implemented in the current version of VASP. Thus Quantum Espresso (version 6.3)[54] was employed for the full-relativistic band structure and SOC density-of-state calculations, using PBE-GGA-PAW-based full-relativistic pseudopotentials (H: H.rel-pbe-kjpaw_psl.1.0.0.UPF; C: C.rel-pbe-n-kjpaw_psl.1.0.0.UPF; N: N.rel-pbe-n-kjpaw_psl.1.0.0.UPF; I: I.rel-pbe-n-kjpaw_psl.1.0.0.UPF; Pb: Pb.rel-pbe-dn-kjpaw_psl.1.0.0.UPF). The optimized geometries obtained in the VASP calculations were taken for all full-relativistic calculations. The kinetic energy cutoff for the plane-wave basis set was 100 Ry (1360.57 eV).

Non-colinear SOC band structure calculations with all-electron pseudopotentials: the non-colinear SOC band structure calculations was also performed with all-electron pseudopotentials, as implemented in the FHI-AIMS software (version 210716_3).[26,55] This was done to check whether the observed band splitting into (R/S-MBA)$_2$PbI$_4$ (Figures 4a,b) is due to the non-colinear SOC effects or due to the PAW-frozen-core approximation of pseudopotentials in the VASP calculations. Both DFT+SOC and DFT-HSE06+SOC ($\alpha = 0.25$ and 0.43) frameworks with the PBE-GGA functional were utilized. Irrespective of the flavor pseudopotentials, consistent band splitting across the DFT packages was obtained.

Effective mass calculation: The effective mass of electron (m_e*)/hole (m_h*) was estimated from the parabolic fitting of the band energy dispersion relation at the top (bottom) of the valence (conduction) band maximum (minimum) following the previous work:[10]

$$m^*_{e/h} = \%\hbar\left[\frac{d^2E(k)}{d^2k}\right]^{-1} \quad (5)$$

where k is the wavevector. E(k) are the band energies obtained from the eigenvalues of an electron in a band at a wavevector k using DFT. No SOC was applied to achieve a better agreement in the parabolic fitting (Figure S15, Supporting Information). First m_e*/m_h* was estimated for (R-MBA)$_2$PbI$_4$ and (S-MBA$_{0.5}n$BA$_{0.5}$)$_2$PbI$_4$. Then those values were used for (S-MBA)$_2$PbI$_4$ and (R-MBA$_{0.5}n$BA$_{0.5}$)$_2$PbI$_4$, as the valence (conduction) band maxima (minima) are similar for R and S chirality for the respective systems.

Supporting Information

Supporting Information is available from the Wiley Online Library or from the author.

Acknowledgements

This work was financially supported by the National Science Foundation (NSF) (EPM-2114350, Q.Y.). T.W. thanks for the support of NSF (Award #: 2118099). This work made use of the Cornell Center for Materials Research Shared Facilities which are supported through the NSF MRSEC program (DMR-1719875) and the GIWAXS from the CMS beamline (11-BM) and temperature-dependent XRD and PDF from the 28ID-2 XPD beamline of the National Synchrotron Light Source II, and the TA and PL spectroscopy resource and the theory and computation resource at the Center for Functional Nanomaterials, both supported by U.S. DOE Office of Science Facilities at Brookhaven National Laboratory under Contract No. DE-SC0012704. M.W.T. gratefully acknowledges support from BASF.

Conflict of Interest

The authors declare no conflict of interest.

Data Availability Statement

The data that support the findings of this study are available from the corresponding author upon reasonable request.

Keywords

2D perovskites, chiral–achiral cation, chiroptoelectronic, spin-polarized band-splitting, structural distortion

Received: July 5, 2024
Revised: August 22, 2024
Published online:

[1] a) G. Long, R. Sabatini, M. I. Saidaminov, G. Lakhwani, A. Rasmita, X. Liu, E. H. Sargent, W. Gao, *Nat. Rev. Mater.* **2020**, *5*, 423; b) S. Ma, J. Ahn, J. Moon, *Adv. Mater.* **2021**, *33*, 2005760; c) H. Lu, Z. V. Vardeny, M. C. Beard, *Nat. Rev. Chem.* **2022**, *6*, 470.
[2] D. G. Billing, A. Lemmerer, *CrystEngComm* **2006**, *8*, 686.
[3] M. K. Jana, R. Song, H. Liu, D. R. Khanal, S. M. Janke, R. Zhao, C. Liu, Z. Valy Vardeny, V. Blum, D. B. Mitzi, *Nat. Commun.* **2020**, *11*, 4699.
[4] R. C. Hilborn, *Am. J. Phys.* **1982**, *50*, 982.
[5] M. K. Jana, R. Song, Y. Xie, R. Zhao, P. C. Sercel, V. Blum, D. B. Mitzi, *Nat. Commun.* **2021**, *12*, 4982.
[6] a) J. Ahn, S. Ma, J. Y. Kim, J. Kyhm, W. Yang, J. A. Lim, N. A. Kotov, J. Moon, *J. Am. Chem. Soc.* **2020**, *142*, 4206; b) H. Lu, C. Xiao, R. Song, T. Li, A. E. Maughan, A. Levin, R. Brunecky, J. J. Berry, D. B. Mitzi, V. Blum, M. C. Beard, *J. Am. Chem. Soc.* **2020**, *142*, 13030.
[7] a) C. Zhou, Y. Chu, L. Ma, Y. Zhong, C. Wang, Y. Liu, H. Zhang, B. Wang, X. Feng, X. Yu, X. Zhang, Y. Sun, X. Li, G. Zhao, *Phys. Chem. Chem. Phys.* **2020**, *22*, 17299; b) J. T. Lin, D. G. Chen, L. S. Yang, T. C. Lin, Y. H. Liu, Y. C. Chao, P. T. Chou, C. W. Chiu, *Angew. Chem., Int. Ed. Engl.* **2021**, *60*, 21434; c) J. Son, S. Ma, Y. K. Jung, J. Tan, G. Jang, H. Lee, C. Lee, J. Lee, S. Moon, W. Jeong, A. Walsh, J. Moon, *Nat. Commun.* **2023**, *14*, 3124.
[8] L. Yan, M. K. Jana, P. C. Sercel, D. B. Mitzi, W. You, *J. Am. Chem. Soc.* **2021**, *143*, 18114.
[9] S. Wang, J. Ma, W. Li, J. Wang, H. Wang, H. Shen, J. Li, J. Wang, H. Luo, D. Li, *J. Phys. Chem. Lett.* **2019**, *10*, 2546.
[10] I. Dursun, M. Terban, Y. Xu, X. Zhang, S. Ghose, M. Li, P. Sarker, H. Li, M. Cotlet, T. Wei, D. Lu, Q. Yu, *J. Phys. Chem. C* **2023**, *127*, 15423.
[11] Y. H. Kim, Y. Zhai, H. Lu, X. Pan, C. Xiao, E. Gaulding, S. Harvey, J. Berry, Z. Vardeny, J. Luther, M. Beard, *Science* **2021**, *371*, 1129.
[12] J. Ma, C. Fang, C. Chen, L. Jin, J. Wang, S. Wang, J. Tang, D. Li, *ACS Nano* **2019**, *13*, 3659.
[13] H. Lu, J. Wang, C. Xiao, X. Pan, X. Chen, R. Brunecky, J. Berry, K. Zhu, M. Beard, Z. Vardeny, *Sci. Adv.* **2019**, *5*, 0571.

[14] A. Ishii, T. Miyasaka, *Sci. Adv.* **2020**, *6*, 3274.
[15] a) A. Salij, R. H. Goldsmith, R. Tempelaar, *J. Am. Chem. Soc.* **2021**, *143*, 21519; b) Z. Zhang, Z. Wang, H. H. Y. Sung, I. D. Williams, Z. G. Yu, H. Lu, *J. Am. Chem. Soc.* **2022**, *144*, 22242; c) G. Albano, G. Pescitelli, L. Di Bari, *Chem. Rev.* **2020**, *120*, 10145.
[16] a) P. E. Blöchl, *Phys. Rev. B* **1994**, *50*, 17953; b) G. Kresse, D. Joubert, *Phys. Rev. B* **1999**, *59*, 1758.
[17] a) G. Kresse, J. Furthmüller, *Phys. Rev. B* **1996**, *54*, 11169; b) G. Kresse, J. Furthmüller, *Comput. Mater. Sci.* **1996**, *6*, 15.
[18] D. G. Billing, *Acta Crystallogr., Sect. F: Struct. Biol. Commun.* **2002**, *58*, m669.
[19] Y. Xie, R. Song, A. Singh, M. K. Jana, V. Blum, D. B. Mitzi, *J. Am. Chem. Soc.* **2022**, *144*, 15223.
[20] L. Yan, M. K. Jana, P. C. Sercel, D. B. Mitzi, W. You, *J. Am. Chem. Soc.* **2021**, *143*, 18114.
[21] M. Nishio, Y. Umezawa, J. Fantini, M. S. Weiss, P. Chakrabarti, *Phys. Chem. Chem. Phys.* **2014**, *16*, 12648.
[22] a) M. Ledinský, P. Löper, B. Niesen, J. Holovský, S. J. Moon, J. H. Yum, S. De Wolf, A. Fejfar, C. Ballif, *J. Phys. Chem. Lett.* **2015**, *6*, 401; b) Z. Liang, S. Zhang, X. Xu, N. Wang, J. Wang, X. Wang, Z. Bi, G. Xu, N. Yuan, J. Ding, *RSC Adv.* **2015**, *5*, 60562.
[23] a) J. Heyd, G. E. Scuseria, M. Ernzerhof, *J. Chem. Phys.* **2003**, *118*, 8207; b) J. Heyd, G. Scuseria, M. Ernzerhof, *J. Chem. Phys.* **2006**, *124*, 9906.
[24] K.-z. Du, Q. Tu, X. Zhang, Q. Han, J. Liu, S. Zauscher, D. B. Mitzi, *Inorg. Chem.* **2017**, *56*, 9291.
[25] S. Apergi, G. Brocks, S. Tao, *J. Phys. Chem. Lett.* **2023**, *14*, 11565.
[26] V. Blum, R. Gehrke, F. Hanke, P. Havu, V. Havu, X. Ren, K. Reuter, M. Scheffler, *Comput. Phys. Commun.* **2009**, *180*, 2175.
[27] G. Zhan, J. Zhang, L. Zhang, Z. Ou, H. Yang, Y. Qian, X. Zhang, Z. Xing, L. Zhang, C. Li, J. Zhong, J. Yuan, Y. Cao, D. Zhou, X. Chen, H. Ma, X. Song, C. Zha, X. Huang, J. Wang, T. Wang, W. Huang, L. Wang, *Nano Lett.* **2022**, *22*, 3961.
[28] M. A. Pérez-Osorio, R. L. Milot, M. R. Filip, J. B. Patel, L. M. Herz, M. B. Johnston, F. Giustino, *J. Phys. Chem. C* **2015**, *119*, 25703.
[29] A. March, **1932**, *81*, 285.
[30] S. Liu, A. R. DeFilippo, M. Balasubramanian, Z. Liu, S. G. Wang, Y. S. Chen, S. Chariton, V. Prakapenka, X. Luo, L. Zhao, J. S. Martin, Y. Lin, Y. Yan, S. K. Ghose, T. A. Tyson, *Adv. Sci. (Weinh)* **2021**, *8*, 2003046.
[31] a) P. Juhás, T. Davis, C. L. Farrow, S. J. L. Billinge, *J. Appl. Crystallogr.* **2013**, *46*, 560; b) C. L. Farrow, P. Juhás, J. W. Liu, D. Bryndin, E. S. Božin, J. Bloch, T. H. Proffen, S. J. L. Billinge, *J. Phys.: Condens. Matter* **2007**, *19*, 335219.
[32] S. Y. Harouna-Mayer, S. Tao, Z. Gong, M. v. Zimmermann, D. Koziej, A. C. Dippel, S. J. L. Billinge, *IUCrJ* **2022**, *9*, 594.
[33] J. A. Steele, P. Puech, B. Monserrat, B. Wu, R. X. Yang, T. Kirchartz, H. Yuan, G. Fleury, D. Giovanni, E. Fron, M. Keshavarz, E. Debroye, G. Zhou, T. C. Sum, A. Walsh, J. Hofkens, M. B. J. Roeffaers, *ACS Energy Lett.* **2019**, *4*, 2205.
[34] a) K. Marjit, A. G. Francis, S. K. Pati, A. Patra, *J. Phys. Chem. Lett.* **2023**, *14*, 10900; b) X. Hong, T. Ishihara, A. V. Nurmikko, *Phys. Rev. B* **1992**, *45*, 6961.
[35] J. C. Blancon, A. V. Stier, H. Tsai, W. Nie, C. C. Stoumpos, B. Traoré, L. Pedesseau, M. Kepenekian, F. Katsutani, G. T. Noe, J. Kono, S. Tretiak, S. A. Crooker, C. Katan, M. G. Kanatzidis, J. J. Crochet, J. Even, A. D. Mohite, *Nat. Commun.* **2018**, *9*, 2254.
[36] A. D. Wright, C. Verdi, R. L. Milot, G. E. Eperon, M. A. Perez-Osorio, H. J. Snaith, F. Giustino, M. B. Johnston, L. M. Herz, *Nat. Commun.* **2016**, *7*, 11755.
[37] R. Chen, D. Li, B. Liu, Z. Peng, G. G. Gurzadyan, Q. Xiong, H. Sun, *Nano Lett.* **2010**, *10*, 4956.
[38] a) J. Bhosale, A. K. Ramdas, A. Burger, A. Muñoz, A. H. Romero, M. Cardona, R. Lauck, R. K. Kremer, *Phys. Rev. B* **2012**, *86*, 195208; b) S. Wang, J. Ma, W. Li, J. Wang, H. Wang, H. Shen, J. Li, J. Wang, H. Luo, D. Li, *J. Phys. Chem. Lett.* **2019**, *10*, 2546.
[39] a) D. R. Kripalani, Y. Cai, J. Lou, K. Zhou, *ACS Nano* **2022**, *16*, 261; b) Z. Zhang, S. Ghimire, T. Okamoto, B. M. Sachith, J. Sobhanan, C. Subrahmanyam, V. Biju, *ACS Nano* **2022**, *16*, 160; c) D. Dai, R. Shi, R. Long, *J. Phys. Chem. Lett.* **2022**, *13*, 2718.
[40] Z. Guo, X. Wu, T. Zhu, X. Zhu, L. Huang, *ACS Nano* **2016**, *10*, 9992.
[41] K. Kaasbjerg, K. S. Thygesen, K. W. Jacobsen, *Phys. Rev. B* **2012**, *85*, 115317.
[42] M. B. Price, J. Butkus, T. C. Jellicoe, A. Sadhanala, A. Briane, J. E. Halpert, K. Broch, J. M. Hodgkiss, R. H. Friend, F. Deschler, *Nat. Commun.* **2015**, *6*, 8420.
[43] H. Li, Y. Xu, S. Ramakrishnan, Y. Zhang, M. Cotlet, T. L. Xu, Q. Yu, *Cell Rep. Phys. Sci.* **2022**, *3*, 101060.
[44] a) J. P. Perdew, J. A. Chevary, S. H. Vosko, K. A. Jackson, M. R. Pederson, D. J. Singh, C. Fiolhais, *Phys. Rev. B* **1992**, *46*, 6671; b) J. P. Perdew, K. Burke, M. Ernzerhof, *Phys. Rev. Lett.* **1996**, *77*, 3865.
[45] S. Grimme, J. Antony, S. Ehrlich, H. Krieg, *J. Chem. Phys.* **2010**, *132*, 154104.
[46] H. J. Monkhorst, J. D. Pack, *Phys. Rev. B* **1976**, *13*, 5188.
[47] a) K. Momma, F. Izumi, *J. Appl. Crystallogr.* **2008**, *41*, 653; b) F. Izumi, K. Momma, *Solid State Phenom.* **2007**, *130*, 15.
[48] H. T. Stokes, D. M. Hatch, *J. Appl. Crystallogr.* **2005**, *38*, 237.
[49] W. Setyawan, S. Curtarolo, *Comput. Mater. Sci.* **2010**, *49*, 299.
[50] E. I. Marchenko, S. A. Fateev, A. A. Petrov, V. V. Korolev, A. Mitrofanov, A. V. Petrov, E. A. Goodilin, A. B. Tarasov, *Chem. Mater.* **2020**, *32*, 7383.
[51] a) T. Sheikh, S. Maqbool, P. K. Rajput, P. Mandal, A. Nag, *Chem. Commun.* **2022**, *58*, 7650; b) Y. Dang, X. Liu, Y. Sun, J. Song, W. Hu, X. Tao, *J. Phys. Chem. Lett.* **2020**, *11*, 1689.
[52] a) P. Sarker, M. N. Huda, *Comput. Mater. Sci.* **2016**, *111*, 359; b) P. Sarker, M. M. Al-Jassim, M. N. Huda, *Appl. Phys. Lett.* **2015**, *107*, 233902; c) P. Sarker, D. Prasher, N. Gaillard, M. N. Huda, *J. Appl. Phys.* **2013**, *114*, 133508; d) N. R. de Tacconi, H. K. Timmaji, W. Chanmanee, M. N. Huda, P. Sarker, C. Janáky, K. Rajeshwar, *ChemPhysChem* **2012**, *13*, 2945.
[53] P. Sarker, M. N. Huda, *Comput. Mater. Sci.* **2016**, *111*, 359.
[54] P. Giannozzi, S. Baroni, N. Bonini, M. Calandra, R. Car, C. Cavazzoni, D. Ceresoli, G. L. Chiarotti, M. Cococcioni, I. Dabo, A. Dal Corso, S. de Gironcoli, S. Fabris, G. Fratesi, R. Gebauer, U. Gerstmann, C. Gougoussis, A. Kokalj, M. Lazzeri, L. Martin-Samos, N. Marzari, F. Mauri, R. Mazzarello, S. Paolini, A. Pasquarello, L. Paulatto, C. Sbraccia, S. Scandolo, G. Sclauzero, A. P. Seitsonen, et al., *J. Phys.: Condens. Matter* **2009**, *21*, 395502.
[55] a) V. Yu, F. Corsetti, A. García, W. Huhn, M. Jacquelin, W. Jia, B. Lange, L. Lin, J. Lu, W. Mi, A. Seifitokaldani, Á. Vázquez-Mayagoitia, C. Yang, H. Yang, V. Blum, *Comput. Phys. Commun.* **2017**, *222*, 267; b) V. Havu, V. Blum, P. Havu, M. Scheffler, *J. Comput. Phys.* **2009**, *228*, 8367; c) W. Huhn, V. Blum, *Phys. Rev. Mater.* **2017**, *1*, 033803.